INTERNATIONAL JOURNAL FOR NUMERICAL METHODS IN FLUIDS
Int. J. Numer. Meth. Fluids 2010; **62**:138–165

Simulation of multiple shock–shock interference using implicit anti-diffusive WENO schemes

Tsang-Jen Hsieh[1], Ching-Hua Wang[1] and Jaw-Yen Yang[2,*,†,‡]

[1]*Department of Mechanical Engineering, National Taiwan University, Taipei, Taiwan*
[2]*Institute of Applied Mechanics, National Taiwan University, Taipei, Taiwan*

SUMMARY

Accurate computations of two-dimensional turbulent hypersonic shock–shock interactions that arise when single and dual shocks impinge on the bow shock in front of a cylinder are presented. The simulation methods used are a class of lower–upper symmetric-Gauss–Seidel implicit anti-diffusive weighted essentially non-oscillatory (WENO) schemes for solving the compressible Navier–Stokes equations with Spalart–Allmaras one-equation turbulence model. A numerical flux of WENO scheme with anti-diffusive flux correction is adopted, which consists of first-order and high-order fluxes and allows for a more flexible choice of first-order dissipative methods. Experimental flow fields of type IV shock–shock interactions with single and dual incident shocks by Wieting are computed. By using the WENO scheme with anti-diffusive flux corrections, the present solution indicates that good accuracy is maintained and contact discontinuities are sharpened markedly as compared with the original WENO schemes on the same meshes. Computed surface pressure distribution and heat transfer rate are also compared with experimental data and other computational results and good agreement is found. Copyright © 2009 John Wiley & Sons, Ltd.

Received 24 October 2008; Revised 31 December 2008; Accepted 7 January 2009

KEY WORDS: compressible viscous flow; hypersonic shock–shock interaction; anti-diffusive WENO; contact discontinuity sharpening; turbulent flow; implicit method

1. INTRODUCTION

The flow around a hypersonic vehicle is generally characterized by complex shock–shock and shock-boundary layer interactions. Type IV shock–shock interaction is one of six types of shock interactions first categorized by Edney [1] and is known as the most critical one due to its creation of potentially destructive local peaks of pressure and heat flux. The type IV supersonic

---

*Correspondence to: Jaw-Yen Yang, Institute of Applied Mechanics, National Taiwan University, Taipei, Taiwan.
†E-mail: yangjy@spring.iam.ntu.edu.tw
‡AIAA member.

Contract/grant sponsor: National Science Council; contract/grant number: NSC-97-2212-E002-055

jet interference pattern, shown in Figure 1, occurs when an oblique shock wave intersects the nearly normal part of the bow shock formed from a blunt leading edge. The intersection results in further displacement of the bow shock wave and forms a supersonic jet contained between two shear layers and submerged within the subsonic shock layer between the body and the bow shock wave. A jet bow shock is produced when the jet impinges on the surface, creating a small region of stagnation heating. The maximum pressure and heat transfer rates are found to occur when the jet impinges perpendicularly to the surface. Experimental studies of type IV interactions generated by single incident shock have been reported in [2–4]. Holden *et al.* [5] and Wieting [6] have reported experiments on type IV interaction in the presence of dual incident shocks. This new interference pattern is shown schematically in Figure 2. More complicated interaction patterns are generated in this case. This type of interference pattern obtained is found to depend on the strength of the impinging shock waves and their interaction points on the body's bow shock wave. The pressure and heat transfer rate amplifications are dependent on both the interference pattern and the flow angle of incidence with surface. A more recent theoretical and experimental study

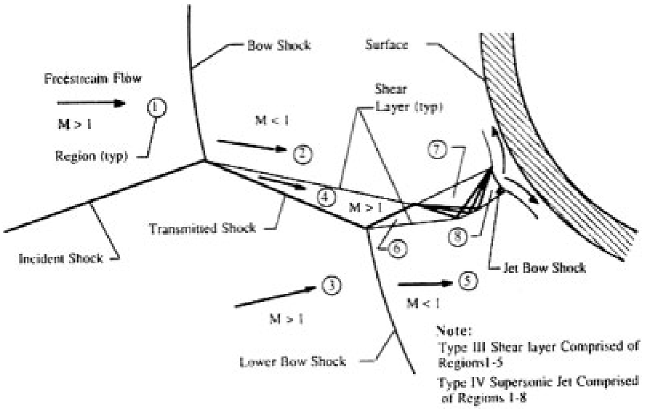

Figure 1. Schematic of type IV supersonic jet interference pattern [6].

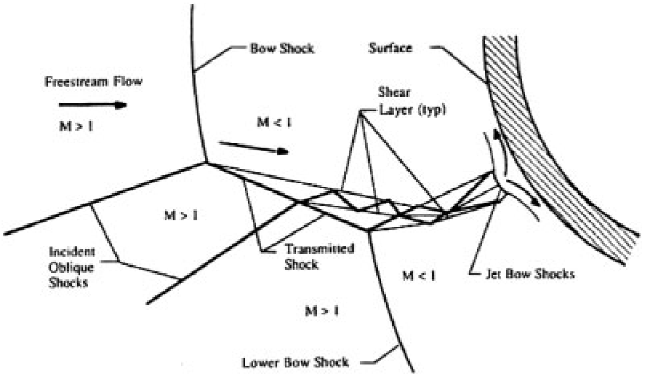

Figure 2. Schematic of concomitant supersonic jet interference pattern [6].

DOI: 10.1002/fld

on type III and type IV shock–shock interferences can be found in [7] for slightly higher Mach numbers. Several numerical studies on type IV shock–shock interaction have been reported [8–12]. It was found that the pressure peak, heat transfer rates, and pressure distributions are sensitive to the upstream thermodynamic flow conditions, shock strength, and Mach number. It was also indicated that type IV interaction may be unsteady. The unsteadiness is shown to be caused by the generation of vortices shed from both the upper and the lower surfaces of the impinging jet. It was also found that the shear-layer turbulence and viscous effects play an important role on the jet structure in shock–shock interference, see Holden and Kolly [13]. To compute these hypersonic type IV shock–shock interactions requires not only the capability of accurate and stable shock resolution and capturing but also the capability of accurate resolution of contact discontinuities or slip lines as well as adequate turbulence models due to the dominant dual-jet and the concomitant jet features.

The weighted essentially non-oscillatory (WENO) schemes proposed by Liu *et al.* [14] and extended by Jiang and Shu [15] for solving hyperbolic conservation laws have been widely and successfully applied to many science and engineering fields for the past two decades. Implicit versions of WENO schemes for solving the Euler and Navier–Stokes equations have been successfully applied to incompressible and compressible flow problems by Yang *et al.* [16–19]. Good convergence rate to steady-state solution using implicit WENO schemes has been illustrated as compared with that of implicit essentially non-oscillatory schemes.

In recent years, several variants and improvements of the original WENO schemes [14, 15] have been proposed [20–24]. By introducing an anti-diffusive flux, Despres and Lagoutiere [20] proposed a first-order approach called limited downwind scheme to prevent the smearing of contact discontinuities while keeping nonlinear stability. Later Bouchut [21] modified this scheme to satisfy entropy conditions and also gave a simple explicit formula for this limited downwind anti-diffusive flux. As inspired by these works [20, 21], Xu and Shu [22] developed an anti-diffusive flux correction technique based on high-order finite difference WENO schemes; the resulting scheme maintains high-order accuracy in smooth regions, non-oscillatory behavior near discontinuities, and sharp contact discontinuity resolution. Also, a mapped WENO scheme has been devised by Henrick *et al.* [23] that improves over the original WENO scheme at critical points. Zhang and Shu [24] suggested a modified smoothness indicator for the fifth-order WENO scheme near a steady shock region and they showed that the residue for the WENO scheme with the new smoothness indicator can converge to machine zero for one- and two-dimensional steady problems with strong shock wave when there is no influence from the boundary conditions. Recently, a numerical comparison of several variant WENO schemes for the compressible Euler equations has been given [25], which includes a lower–upper Gauss–Seidel implicit WENO scheme with anti-diffusive flux. Also, in [26], an implicit WENO scheme with anti-diffusive flux is adopted for the compressible Navier–Stokes equations for computing viscous steady-state flows. A numerical flux of WENO scheme in flux limiter form is presented, which consists of first-order and high-order fluxes and allows for a more flexible choice of first-order dissipative entropy satisfying methods. Many first-order dissipative schemes can be used. Besides shock resolution, we also aim at improving the resolution of contact discontinuities (or slip lines) and their subsequent evolution and possible interaction with other flow structures such as shock waves.

For turbulent flow calculations, the Spalart–Allmaras one-equation turbulence model [27], simplified by dropping the transition terms, is adopted, which is based on the transport of eddy viscosity. The model provides a desirable tool for numerical computation of flow involving complex

DOI: 10.1002/fld

geometry. The performance of this model has been tested through comparison with experimental data of several well-documented flow cases.

The main purpose of this work is to compute the complex flow structures of type IV shock–shock interaction, which are full of shock waves and contact discontinuities and their interactions by using our recent implicit anti-diffusive WENO Navier–Stokes solver, which possesses several desirable features including good accuracy in smooth region, good shock capturing and resolution, and better resolution of slip lines (or contact discontinuities) [26]. To treat shear layer and turbulence, the Spalart–Allmaras turbulence model was employed. The structures of two new patterns reported by Wieting [6], namely, concomitant jets and dual type IV jets, are computed. Present numerical results are compared with experiment [6] and other available computational results [13].

2. GOVERNING EQUATIONS

The governing equations are the unsteady Reynolds-averaged compressible Navier–Stokes equations, which express the conservations of mass, momentum, and energy for a viscous fluid. The Spalart–Allmaras one-equation turbulence model as devised in [27] is adopted. In the Cartesian coordinates, the two-dimensional governing equations are given by

$$\frac{\partial Q}{\partial t}+\frac{\partial E}{\partial x}+\frac{\partial F}{\partial y}=\frac{\partial E_v}{\partial x}+\frac{\partial F_v}{\partial y}+H \tag{1}$$

where

$$Q=(\rho,\rho u,\rho v,e,\tilde{v})^{\mathrm{T}}$$

$$E=(\rho u,\rho u^2+p,\rho uv,(e+p)u,\tilde{v}u)^{\mathrm{T}},\quad F=(\rho v,\rho vu,\rho v^2+p,(e+p)v,\tilde{v}v)^{\mathrm{T}} \tag{2}$$

$$E_v=\frac{1}{Re_\infty}\left(0,\tau_{xx},\tau_{xy},E_{v4},f_{v5}\frac{\partial\tilde{v}}{\partial x}\right)^{\mathrm{T}},\quad F_v=\frac{1}{Re_\infty}\left(0,\tau_{xy},\tau_{yy},F_{v4},f_{v5}\frac{\partial\tilde{v}}{\partial y}\right)^{\mathrm{T}} \tag{3}$$

with

$$E_{v4}=u\tau_{xx}+v\tau_{xy}-q_x,\quad F_{v4}=u\tau_{xy}+v\tau_{yy}-q_y$$

$$H=(0,0,0,0,H_5)^{\mathrm{T}}$$

and

$$f_{v5}=\frac{1}{\sigma_\varepsilon}\left(\frac{\mu_l}{\rho}+(1+C_{B2})\tilde{v}\right)$$

In the preceding equations, ρ is the density, u, v the velocity components, e the energy per unit area, and the turbulent variable $\tilde{v}$ would be defined later. The pressure p is related to the dependent

DOI: 10.1002/fld

variables by the equation of state for a perfect gas

$$p=(\gamma-1)[e-\rho(u^2+v^2)/2] \tag{4}$$

where γ is the ratio of specific heats. The heat flux terms are given by

$$q_j=-(K_l+K_t)\frac{\partial T}{\partial x_j}, \quad j=1,2 \tag{5}$$

$$K_l=\frac{\mu_l}{(\gamma-1)M_\infty^2 Pr_l}, \quad K_t=\frac{\mu_t}{(\gamma-1)M_\infty^2 Pr_t}$$

where $Pr=0.72$ and $Pr_t=0.9$ for air. The viscous stress tensors are obtained from

$$\tau_{ij}=(\mu_l+\mu_t)\left(S_{ij}-\frac{1}{3}\frac{\partial u_k}{\partial x_k}\delta_{ij}\right)$$

$$S_{ij}=\frac{1}{2}\left(\frac{\partial u_i}{\partial x_j}+\frac{\partial u_j}{\partial x_i}\right)$$

where $i,j=1,2$ indicate the two coordinate directions. The molecular viscosity μ_l is calculated by Sutherland's law.

The Spalart–Allmaras model is an eddy viscosity model based on a transport equation for turbulent viscosity. The model was devised to improve the predictions obtained with algebraic mixing-length models, to develop a local model for complex flows, and to provide a simpler alternative to two-equation turbulence models. The eddy viscosity function is defined in terms of a non-dimensional eddy viscosity variable, $\tilde{v}$, and a wall damping function f_{v1}, as follows:

$$v_t=\rho\tilde{v}f_{v1}$$

The non-dimensional convective transport equation of the eddy viscosity is modeled as

$$\begin{aligned}\frac{\partial\tilde{v}}{\partial t}+\frac{\partial\tilde{v}u_j}{\partial x_j}&=C_{b1}(1-f_{t2})S\tilde{v}+\frac{1}{Re_\infty\sigma_\varepsilon}\left[\frac{\partial}{\partial x_j}\left((v+\tilde{v})\frac{\partial v}{\partial x_j}\right)+C_{b2}\frac{\partial\tilde{v}}{\partial x_j}\frac{\partial\tilde{v}}{\partial x_j}\right]\\&\quad-\frac{C_{w1}f_w}{Re_\infty}\left(\frac{\tilde{v}}{d}\right)^2+\frac{C_{b1}f_{t2}}{Re_\infty}d\left(\frac{\tilde{v}}{d}\right)^2+\frac{1}{Re_\infty}f_{t1}\Delta U^2\end{aligned} \tag{6}$$

where the terms on the right-hand side of Equation (6) represent turbulence eddy viscosity production, conservative diffusion, non-conservative diffusion, near wall turbulence destruction, transition damping of production, and transition source of turbulence. The functions to control the laminar region of the shear layer and transition to turbulence are defined with functions f_{t1} and f_{t2} to control the transition damping of production and transition source of turbulence, respectively. Since the location of the transition is not predetermined, and the prediction of trip (start of transition) is beyond the purpose of this paper, we neglect the effects of the transition model, and focus the validated case on laminar or fully turbulent conditions. The last two terms on the right-hand side of Equation (6) are omitted.

In this study, we formulate the convective transport equation for the eddy viscosity in a form with convective term, dissipative term as in Equations (1) and (2), and with the source term expressed as

$$H_5 = C_{b2}(1-f_{t2})\Omega\tilde{v} + \frac{1}{Re_\infty}\left(\frac{C_{b1}f_{v2}}{k^2} - C_{w1}f_w\right)\left(\frac{\tilde{v}}{d}\right)^2 + \frac{1}{Re_\infty}\left(\frac{C_{b2}\tilde{v}}{\sigma_\varepsilon}\right)\nabla^2\tilde{v} \tag{7}$$

The model constants and auxiliary functions as devised in Reference [28] are adopted. The basic model constants for free-shear flow to control the production and diffusion of turbulent eddy viscosity in the boundary layer zone are

$$C_{b1} = 0.1366, \quad C_{b2} = 0.622, \quad \sigma_\varepsilon = \tfrac{2}{3}$$

The additional model constants and auxiliary functions for the destruction of turbulent eddy viscosity in the boundary zone are

$$C_{w1} = C_{b1}/\kappa^2 + (1+C_{b2})/\sigma_\varepsilon, \quad C_{w2} = 0.3, \quad C_{w3} = 2$$

$$r = \frac{\tilde{v}}{Re_\infty S\kappa^2 d^2}, \quad g = r + C_{w2}(r^6 - r), \quad f_w = g\left(\frac{1+C_{w3}^6}{g^6 + C_{w3}^6}\right)^{1/6}$$

For near wall flow regions, the related functions and constants are given by

$$S = \Omega + \frac{\tilde{v} f_{v2}}{Re_\infty \kappa^2 d^2}, \quad \Omega = |u_y - v_x|, \quad \chi = \frac{\tilde{v}}{v_l}$$

$$f_{v2} = 1 - \frac{\chi}{1+\chi f_{v1}}, \quad f_{v1} = \frac{\chi^3}{(\chi^3 + C_{v1}^3)}$$

The model uses distance to the nearest wall d in its formulation and provides smooth laminar-turbulent transition capabilities.

The dimensional quantities (denoted by an overbar) are non-dimensionalized using the free-stream conditions (denoted by ∞) and a characteristic length $\bar{L}$:

$$x = \frac{\bar{x}}{\bar{L}}, \quad y = \frac{\bar{y}}{\bar{L}}, \quad t = \frac{\bar{t}\bar{V}_\infty}{\bar{L}}$$

$$\rho = \frac{\bar{\rho}}{\bar{\rho}_\infty}, \quad u = \frac{\bar{u}}{\bar{V}_\infty}, \quad v = \frac{\bar{v}}{\bar{V}_\infty}$$

$$a = \frac{\bar{a}}{\bar{a}_\infty}, \quad p = \frac{\bar{p}}{\bar{\rho}_\infty \bar{a}_\infty^2}, \quad T = \frac{\bar{T}}{\bar{T}_\infty}$$

$$\mu_l = \frac{\bar{\mu}_l}{\bar{\mu}_{l\infty}}, \quad \mu_t = \frac{\bar{\mu}_t}{\bar{\mu}_{l\infty}}, \quad \tilde{v} = \frac{\bar{\rho}\bar{\tilde{v}}}{\bar{\mu}_{l\infty}}$$

where $\bar{a}_\infty = (\gamma\bar{p}_\infty/\bar{\rho}_\infty)^{1/2}$ is the free-stream speed of sound and $\bar{V}_\infty$ is the reference speed of free-stream status.

DOI: 10.1002/fld

To allow for the development of a discrete control cell formulation, Equation (1) is presented in integral form as

$$\begin{aligned} &\frac{\partial}{\partial t}\left(\frac{1}{S}\int_S Q\,\mathrm{d}S\right)+\frac{1}{S}\oint_L(\Im-\Im_v)\cdot\mathbf{n}\,\mathrm{d}L=H\\ &\Im=E\mathbf{i}+F\mathbf{j}\\ &\Im_v=E_v\mathbf{i}+F_v\mathbf{j}\end{aligned} \tag{8}$$

where S is the area of the cell that is bounded by the boundary L with the outward unit normal $\mathbf{n}$. The area-averaged values for the conservative variable Q and the source term H are defined as follows:

$$\bar{Q}=\frac{1}{S}\int_S Q\,\mathrm{d}S,\quad \bar{H}=\frac{1}{S}\int_S H\,\mathrm{d}S$$

Let $\mathbf{L}^\xi=\mathbf{n}^\xi L^\xi=L_x^\xi\mathbf{i}+L_y^\xi\mathbf{j}$ be the length vector of the cell side in the ξ direction, then the fluxes at generalized coordinates (ξ,η) can be defined as

$$\hat{E}=\Im\cdot\mathbf{L}^\xi=(L_x^\xi E+L_y^\xi F),\quad \hat{E}_v=\Im_v\cdot\mathbf{L}^\xi=(L_x^\xi E_v+L_y^\xi F_v)$$

$$\hat{F}=\Im\cdot\mathbf{L}^\eta=(L_x^\eta E+L_y^\eta F),\quad \hat{F}_v=\Im_v\cdot\mathbf{L}^\eta=(L_x^\eta E_v+L_y^\eta F_v)$$

In the following, we associate the subscripts i,j with ξ,η directions and use the half-integer subscripts to denote cell sides and full integer subscripts the cell itself or its centroid. Equation (8) may be expressed in semi-discrete conservation law form given by

$$\begin{aligned}\left(\frac{\partial\bar{Q}}{\partial t}\right)_{i,j}=&-\frac{1}{S}[(\hat{E}-\hat{E}_v)_{i+1/2,j}-(\hat{E}-\hat{E}_v)_{i-1/2,j}]\\ &-\frac{1}{S}[(\hat{F}-\hat{F}_v)_{i,j+1/2}-(\hat{F}-\hat{F}_v)_{i,j-1/2}]+\bar{H}_{i,j}\end{aligned} \tag{9}$$

where $(\hat{E})_{i+1/2,j}=(\Im\cdot\mathbf{L}^\xi)_{i+1/2,j}=\hat{E}(Q_{i,j},L_{i+1/2,j})$ is the physical flux, evaluated based on the state variables at cell center (i,j) and the length vectors at cell side $(i+1/2,j)$. The rest of the fluxes at cell sides can be similarly computed.

3. NUMERICAL METHOD AND BOUNDARY CONDITIONS

3.1. Spatial discretization

By dropping the averaged notation for convenience, a numerical approximation to Equation (9) may be expressed in the form given by

$$\begin{aligned}\left(\frac{\partial Q}{\partial t}\right)_{i,j}=&-\frac{1}{S}[(\tilde{E}-\tilde{E}_v)_{i+1/2,j}-(\tilde{E}-\tilde{E}_v)_{i-1/2,j}]\\ &-\frac{1}{S}[(\tilde{F}-\tilde{F}_v)_{i,j+1/2}-(\tilde{F}-\tilde{F}_v)_{i,j-1/2}]+H_{i,j}\end{aligned} \tag{10}$$

where $(\tilde{E}, \tilde{F})$ and $(\tilde{E}_v, \tilde{F}_v)$ are, respectively, the numerical or representative inviscid and viscous fluxes at the bounding cell side for which discrete conservation is considered. The spatial differencing adopts WENO schemes [15] for the inviscid convective fluxes $(\tilde{E}, \tilde{F})$ and second-order central differencing for viscous fluxes $(\tilde{E}_v, \tilde{F}_v)$. A WENO5 $(r=3)$ numerical flux at a cell surface $i+\frac{1}{2}$ in direction i can be put into the form of a flux limiter method and is defined by

$$\tilde{E}_{i+1/2,j} = \tilde{E}^{L}_{i+1/2,j} + \tilde{E}^{\mathrm{HW}}_{i+1/2,j} \tag{11}$$

and

$$\tilde{E}^{\pm}_{i+1/2,j} = \tilde{E}^{L\pm}_{i+1/2,j} + \tilde{E}^{\mathrm{HW}\pm}_{i+1/2,j}$$

where $\tilde{E}^L$ is the numerical flux of a first-order dissipative entropy satisfying scheme and $\tilde{E}^{\mathrm{HW}}$ is a high-order flux with WENO5 flux limiter. Here, the Roe scheme with Harten's entropy fix is adopted as

$$\tilde{E}^{L}_{i+1/2,j} = \tilde{E}^{L^+}_{i+1/2,j} + \tilde{E}^{L^-}_{i+1/2,j} \tag{12}$$

where

$$\tilde{E}^{L^+}_{i+1/2,j} = \tfrac{1}{2}[\hat{E}(Q_{i,j}, L_{i+1/2,j}) + (R|\Lambda|R^{-1})_{i+1/2,j} Q_{i,j}]$$

$$\tilde{E}^{L^-}_{i+1/2,j} = \tfrac{1}{2}[\hat{E}(Q_{i+1,j}, L_{i+1/2,j}) - (R|\Lambda|R^{-1})_{i+1/2,j} Q_{i+1,j}]$$

and $\hat{E}(Q_{i,j}, L_{i+1/2,j})$ is physical flux, evaluated based on the state variables at cell center (i, j) and the length vector at cell side $(i+\frac{1}{2}, j)$ as described before. R is the similarity transformation matrix consisting of the right eigenvectors of the Euler system linearized around the Roe-averaged state between $Q_{i+1,j}$ and $Q_{i,j}$.

$\tilde{E}^{\mathrm{HW}}$ is a high-order WENO5 $(r=3)$ flux, defined as

$$\tilde{E}^{\mathrm{HW}}_{i+1/2,j} = \sum_{s=1}^{5} \tilde{E}^{\mathrm{HW}}_{(i+1/2,j),s} \cdot r_s \tag{13}$$

with

$$\tilde{E}^{\mathrm{HW}}_{(i+1/2,j),s} = \tilde{E}^{\mathrm{HW}^+}_{(i+1/2,j),s} + \tilde{E}^{\mathrm{HW}^-}_{(i+1/2,j),s} \tag{14}$$

where

$$\tilde{E}^{\mathrm{HW}^+}_{(i+1/2,j),s} = \tfrac{1}{6}(\omega^+_{0,s} q^+_0 + \omega^+_{1,s} q^+_1 + \omega^+_{2,s} q^+_2)$$

$$\tilde{E}^{\mathrm{HW}^-}_{(i+1/2,j),s} = \tfrac{1}{6}(\omega^-_{0,s} q^-_0 + \omega^-_{1,s} q^-_1 + \omega^-_{2,s} q^-_2)$$

$$q^+_0 = -2\Delta E^+_{(i-3/2,j),s} + 5\Delta E^+_{(i-1/2,j),s}$$

$$q^+_1 = \Delta E^+_{(i-1/2,j),s} + 2\Delta E^+_{(i+1/2,j),s}$$

$$q^+_2 = 4\Delta E^+_{(i+1/2,j),s} - \Delta E^+_{(i+3/2,j),s}$$

$$q^-_0 = \Delta E^-_{(i-1/2,j),s} - 4\Delta E^-_{(i+1/2,j),s}$$

$$q_1^- = -2\Delta E^-_{(i+1/2,j),s} - \Delta E^-_{(i+3/2,j),s}$$

$$q_2^- = -5\Delta E^-_{(i+3/2,j),s} + 2\Delta E^-_{(i+5/2,j),s}$$

where

$$\Delta E^\pm_{(i+1/2,j),s} = l_s \cdot \Delta E^\pm_{i+1/2,j} \tag{15}$$

$$\Delta E^+_{i+1/2,j} = \hat{E}(Q_{i+1,j}, L_{i+1/2,j}) - \tilde{E}^L_{i+1/2,j} \tag{16}$$

$$\Delta E^-_{i+1/2,j} = \tilde{E}^L_{i+1/2,j} - \hat{E}(Q_{i,j}, L_{i+1/2,j}) \tag{17}$$

The weights $\omega^\pm$ are defined by

$$\omega^\pm_{k,s} = \frac{\alpha^\pm_{k,s}}{\alpha^\pm_{0,s} + \alpha^\pm_{1,s} + \alpha^\pm_{2,s}}, \quad k = 0, 1, 2 \tag{18}$$

where

$$\alpha^+_{0,s} = \tfrac{1}{10}(\varepsilon + \mathrm{IS}^+_{0,s})^{-2}, \quad \alpha^+_{1,s} = \tfrac{6}{10}(\varepsilon + \mathrm{IS}^+_{1,s})^{-2}, \quad \alpha^+_{2,s} = \tfrac{3}{10}(\varepsilon + \mathrm{IS}^+_{2,s})^{-2} \tag{19}$$

$$\alpha^-_{0,s} = \tfrac{3}{10}(\varepsilon + \mathrm{IS}^-_{0,s})^{-2}, \quad \alpha^-_{1,s} = \tfrac{6}{10}(\varepsilon + \mathrm{IS}^-_{1,s})^{-2}, \quad \alpha^-_{2,s} = \tfrac{1}{10}(\varepsilon + \mathrm{IS}^-_{2,s})^{-2} \tag{20}$$

Here $\varepsilon = 10^{-10}$ and IS are the smoothness indicators, defined as:

$$\begin{aligned}
\mathrm{IS}^+_{0,s} &= \tfrac{13}{12}(-\Delta E^+_{(i-3/2,j),s} + \Delta E^+_{(i-1/2,j),s})^2 + \tfrac{1}{4}(-\Delta E^+_{(i-3/2,j),s} + 3\Delta E^+_{(i-1/2,j),s})^2 \\
\mathrm{IS}^+_{1,s} &= \tfrac{13}{12}(-\Delta E^+_{(i-1/2,j),s} + \Delta E^+_{(i+1/2,j),s})^2 + \tfrac{1}{4}(-\Delta E^+_{(i-1/2,j),s} - \Delta E^+_{(i+1/2,j),s})^2 \\
\mathrm{IS}^+_{2,s} &= \tfrac{13}{12}(-\Delta E^+_{(i+1/2,j),s} + \Delta E^+_{(i+3/2,j),s})^2 + \tfrac{1}{4}(-3\Delta E^+_{(i+1/2,j),s} + \Delta E^+_{(i+3/2,j),s})^2
\end{aligned} \tag{21}$$

$$\begin{aligned}
\mathrm{IS}^-_{0,s} &= \tfrac{13}{12}(-\Delta E^-_{(i-1/2,j),s} + \Delta E^-_{(i+1/2,j),s})^2 + \tfrac{1}{4}(-\Delta E^-_{(i-1/2,j),s} + 3\Delta E^-_{(i+1/2,j),s})^2 \\
\mathrm{IS}^-_{1,s} &= \tfrac{13}{12}(-\Delta E^-_{(i+1/2,j),s} + \Delta E^-_{(i+3/2,j),s})^2 + \tfrac{1}{4}(-\Delta E^-_{(i+1/2,j),s} - \Delta E^-_{(i+3/2,j),s})^2 \\
\mathrm{IS}^-_{2,s} &= \tfrac{13}{12}(-\Delta E^-_{(i+3/2,j),s} + \Delta E^-_{(i+5/2,j),s})^2 + \tfrac{1}{4}(-3\Delta E^-_{(i+3/2,j),s} + \Delta E^-_{(i+5/2,j),s})^2
\end{aligned} \tag{22}$$

In the above, r_s (column vector) and l_s (row vector) are the sth right and left eigenvectors of the Jacobian matrices and they are evaluated using the Roe averages. The r_s and l_s used in Equations (13) and (15), respectively, are evaluated consistently at the $i+\frac{1}{2}$ interface.

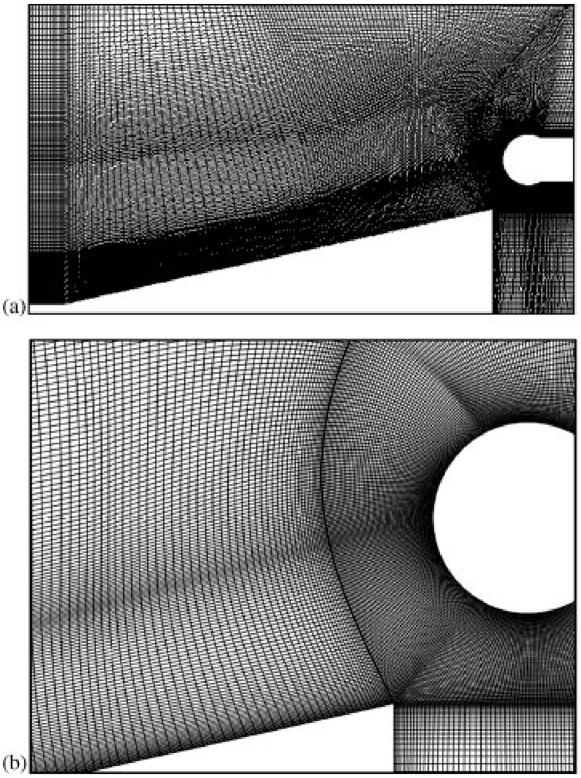

Figure 3. The grid system for run 21: (a) calculation domain and (b) close-up view of the grid in front of the cylinder.

3.2. *Anti-diffusive flux corrections for WENO schemes*

The purpose of the anti-diffusive flux corrections is to improve the resolution of contact discontinuities without sacrificing the accuracy and stability of the original WENO scheme. Equation (11) can be written as an anti-diffusive flux in the following form:

$$\begin{aligned}\tilde{E}^{a}_{i+1/2,j} &= \tilde{E}^{L}_{i+1/2,j} + \tilde{E}^{\mathrm{HW}}_{i+1/2,j}\\ &\quad + \varphi_i \cdot \min\bmod \left(\frac{\hat{E}_{i,j} - \hat{E}_{i-1,j}}{\lambda} + \tilde{E}^{-}_{i-1/2,j} - \tilde{E}^{-}_{i+1/2,j},\ \tilde{E}^{+}_{i+1/2,j} - \tilde{E}^{-}_{i+1/2,j} \right) \end{aligned} \tag{23}$$

where $\lambda = \Delta t/\Delta x$ and φ_i is the discontinuity indicator with its value between 0 and 1, and is defined by

$$\varphi_i = \frac{\beta_i}{\beta_i + \gamma_i}$$

DOI: 10.1002/fld

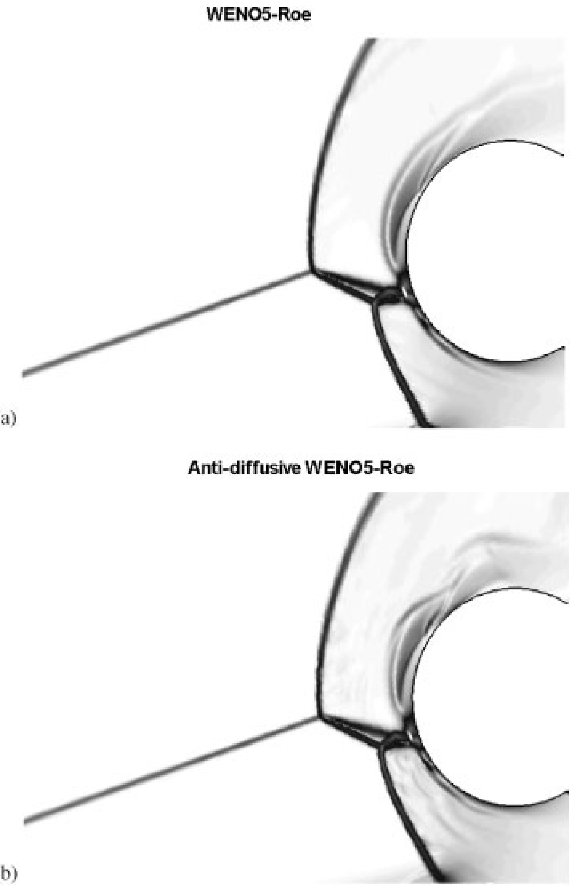

Figure 4. $\nabla\rho$ contours using (a) original WENO5 scheme and (b) WENO5-AD scheme.

where

$$\beta_i=\left(\frac{\alpha_i}{\alpha_{i-1}}+\frac{\alpha_{i+1}}{\alpha_{i+2}}\right)^2,\quad \gamma_i=\frac{|\hat{E}_{i\,\max}-\hat{E}_{i\,\min}|^2}{\alpha_i},\quad \alpha_i=(|\hat{E}_{i-1}-\hat{E}_i|+\varsigma)^2$$

with ς being a small positive number taken as 10^{-6}.

3.3. *Time discretization*

An unfactored implicit scheme can be obtained from a nonlinear implicit scheme by linearizing the flux vectors about the previous time step and dropping the terms of the second and higher orders

$$\begin{aligned}\left[I+\frac{\Delta t}{S}(\delta_\xi\hat{A}+\delta_\eta\hat{B})\right][I-\Delta t\hat{D}]\Delta Q_{i,j}=&-\frac{\Delta t}{S}[(\tilde{E}-\tilde{E}_v)^n_{i+1/2,j}-(\tilde{E}-\tilde{E}_v)^n_{i-1/2,j}]\\&-\frac{\Delta t}{S}[(\tilde{F}-\tilde{F}_v)^n_{i,j+1/2}-(\tilde{F}-\tilde{F}_v)^n_{i,j-1/2}]\\&+\Delta t H_{i,j}\equiv\text{RHS}\end{aligned}\qquad(24)$$

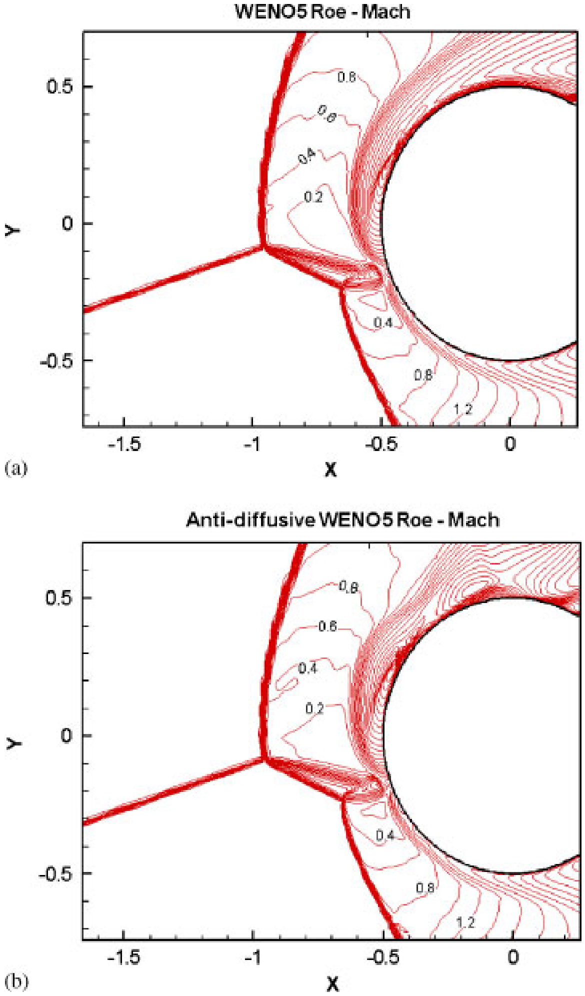

Figure 5. Mach number contours using (a) original WENO5 scheme and (b) WENO5-AD scheme.

where I is the identity matrix, n the time level, δ_ξ, δ_η the difference operators, $\hat{A}$, $\hat{B}$ are the Jacobian matrices of inviscid fluxes, $\hat{D}=\partial H/\partial Q$, and $\Delta Q = Q^{n+1}-Q^n$ is the increment of conservative variables. It is noted that the viscous terms are treated explicitly and the turbulent source functions are treated implicitly. Since the production term is positive, its linearization is not possible; however, there is a strong coupling among the flow field, turbulent viscosity, and the production term.

The matrix inversion resulting from the source-term linearization is performed before the spatial sweeps.

$$\left[I+\frac{\Delta t}{S}(\delta_\xi \hat{A}+\delta_\eta \hat{B})\right]\Delta Q_{i,j}=\mathrm{RHS}/[I-\Delta t\hat{D}]\equiv \mathrm{RHS}^* \tag{25}$$

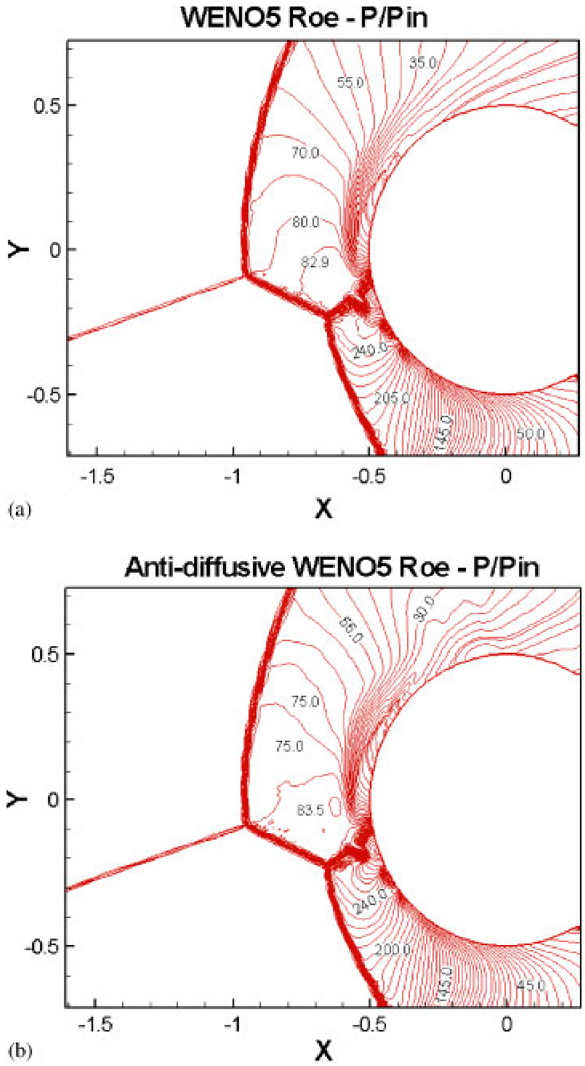

Figure 6. Pressure contours using (a) WENO5 scheme and (b) WENO5-AD scheme.

The LU-SGS (lower–upper symmetric-Gauss–Seidel) implicit factorization scheme of Yoon and Jameson [29] for Equation (25) can be derived by combining the advantages of LU factorization and SGS relaxation. The LU-SGS scheme can be written as

$$LD^{-1}U\Delta Q = \text{RHS}^* \tag{26}$$

where the operators, L, D, and U are defined similarly to that in [29]. Equation (26) can be inverted in three steps

$$\Delta Q^* = L^{-1}\text{RHS}^* \tag{27}$$

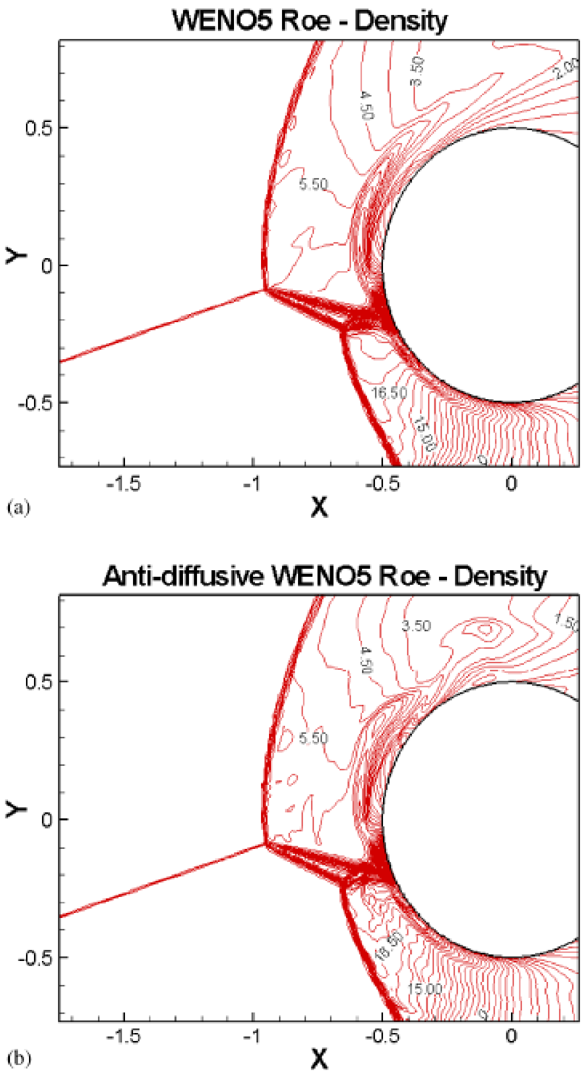

Figure 7. Density contours: (a) original WENO5 scheme and (b) WENO5-AD scheme.

$$\Delta Q^{**} = DQ^{*} \tag{28}$$

$$\Delta Q = U^{-1} Q^{**} \tag{29}$$

It is noted that the present implicit algorithm (LU-SGS) is completely vectorizable on $i+j=$ constant oblique plane of sweep.

3.4. Boundary conditions

The mean flow and turbulent transport equations presented in the preceding sections represent an initial-boundary value problem. In order to solve these equations, it is necessary to impose initial

DOI: 10.1002/fld

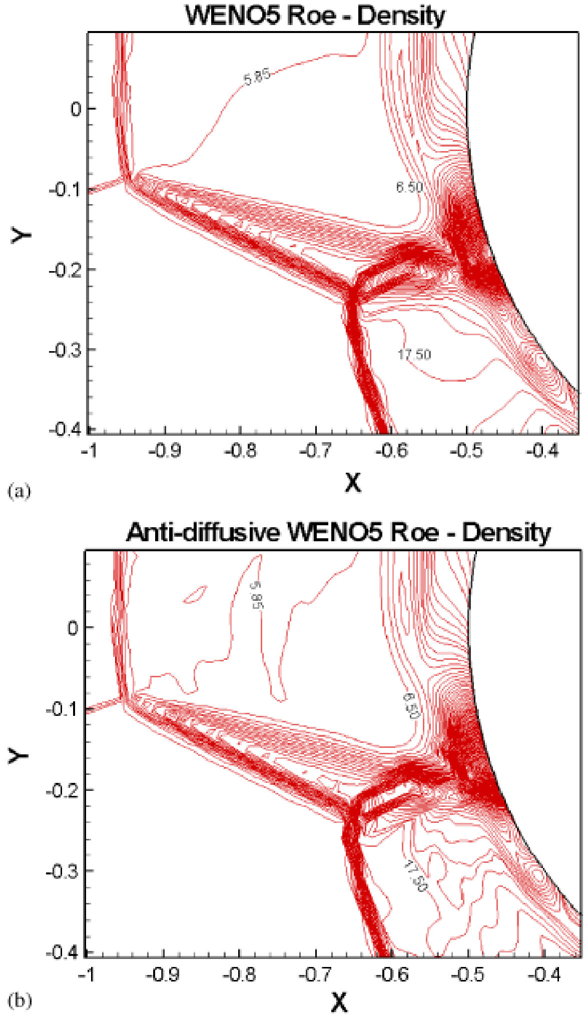

Figure 8. Density contours: (a) original WENO5 scheme locally enlarged view and (b) WENO5-AD scheme, locally enlarged view.

and boundary conditions. A uniform flow field is chosen as the initial conditions for the mean flow equations. A uniform value of $v_t \approx 1000$ is set as the initial guess.

Boundary conditions of the mean flow are set as follows: (1) No slip boundary conditions for velocities are adopted on the solid surface that is assumed to be an adiabatic wall. (2) The density and pressure on the wall are set to be equal to values of the node points next to the wall. This gives first-order accuracy at the wall. (3) In the far field, a locally one-dimensional characteristic type of boundary condition is used. For the turbulent transport equation, a zeroth-order extrapolation is used to specify conditions at the far field.

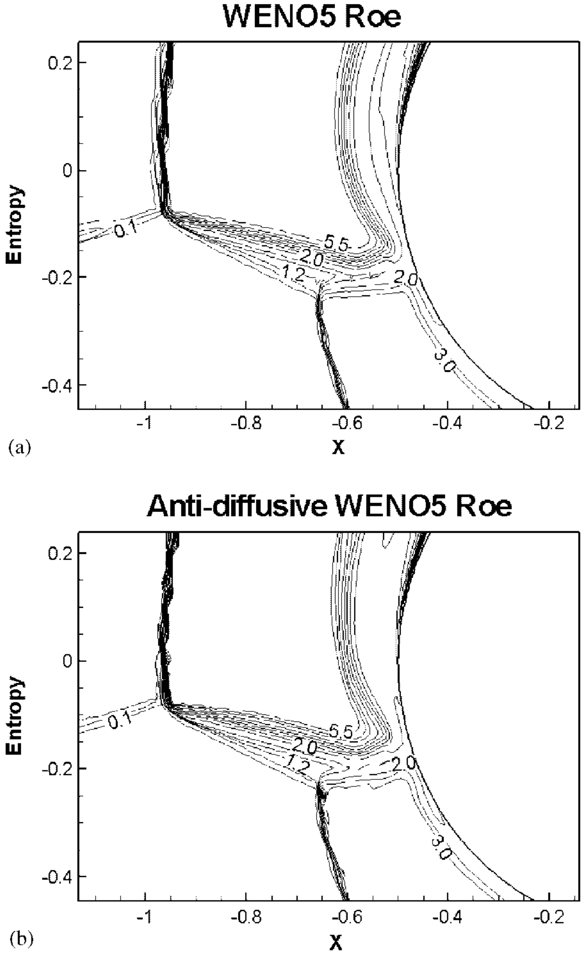

Figure 9. Entropy contours using (a) original WENO5 scheme and (b) WENO5-AD scheme.

4. RESULTS AND DISCUSSION

The present numerical study consists of two types of simulations. In the first case, the simulation for run 21 in Reference [6] was considered, which included type IV interactions generated by single incident shock. In the second case, the simulation for run 87 in Reference [6] was considered, which included type IV interactions generated by dual incident shocks. A multi-block grid system that wraps around the front face of the cylinder is used in our computations. The domain is large enough to include the shock generator and all the interactions in the nose region of the cylinder. For viscous calculations, grid concentration toward the wall surface is added to resolve the boundary layer. The flow domain of interest is bounded by inflow, outflow, and wall boundary. For simplicity of boundary-point procedures, the inflow and outflow boundaries are chosen in such a way that the

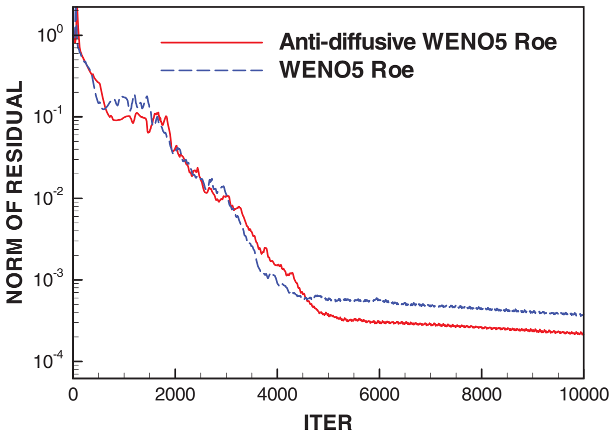

Figure 10. The convergent histories of WENO5 and WENO5-AD.

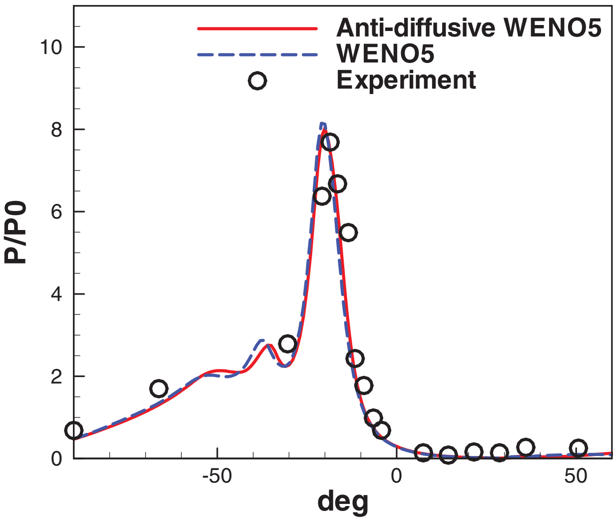

Figure 11. Pressure distributions along the circumference of the cylinder.

flow is always supersonic. No slip wall boundary conditions are used for viscous flow calculations. An isothermal wall boundary with wall temperature $T_w = 290°K$ is specified in order to be able to compare the calculated heat transfer data with those from the experiment.

Two numerical schemes were employed to simulate the following flow fields, one is the WENO5 method (with $r = 3$) and with Roe's method for the first-order scheme, which we denote as WENO5 and the second scheme is based on the WENO5 and augmented with anti-diffusive flux, which we denote as WENO5-AD.

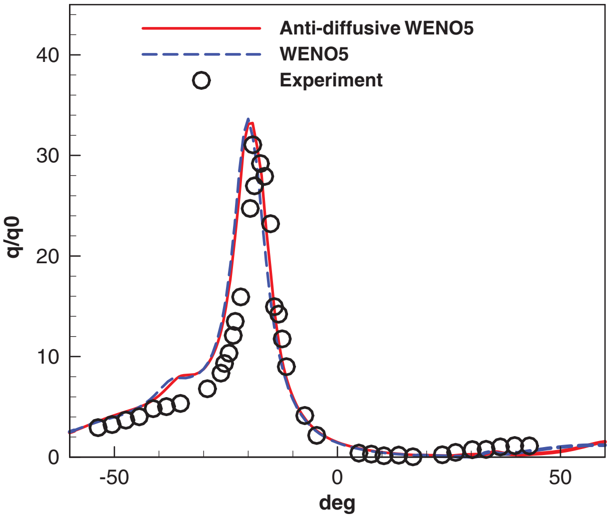

Figure 12. Heat transfer rate distributions along the circumference of the cylinder.

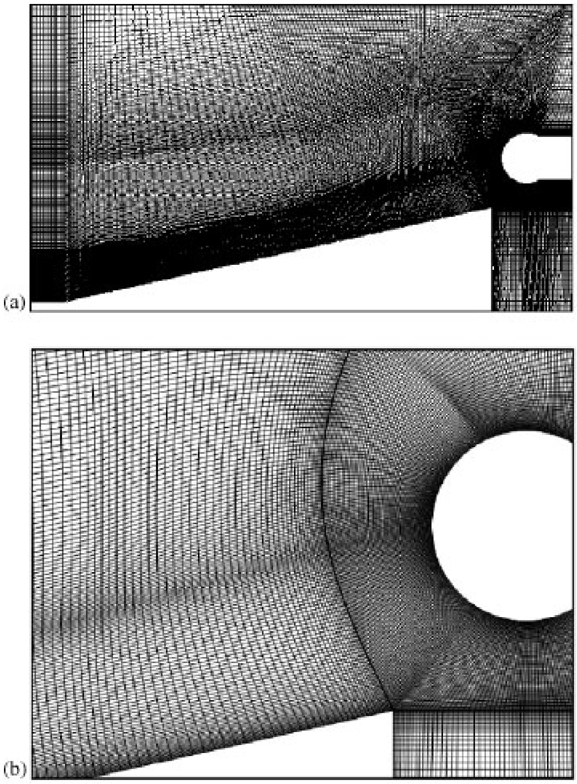

Figure 13. The grid system for run 87: (a) calculation domain and (b) close-up view of the grid in front of the cylinder.

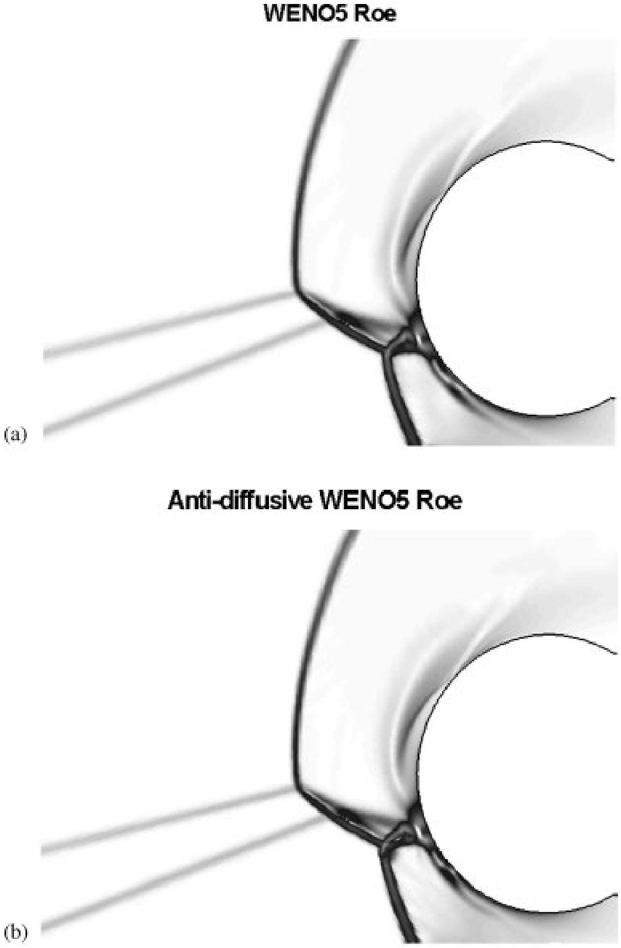

Figure 14. Dual incident shock, type IV interference. $\nabla\rho$ contours using: (a) original WENO5 scheme and (b) WENO5-AD scheme.

5. TYPE IV INTERACTIONS GENERATED BY SINGLE INCIDENT SHOCK

The free-stream conditions chosen for the simulation were $M_\infty = 8.03$, $Re = 5.12\times 10^6$, $P_\infty = 0.875\,\mathrm{kpa}$, and $T_\infty = 122^\circ\mathrm{K}$. The type IV interaction generated by single incident shock occurs when an oblique shock wave intersects the nearly normal part of the bow shock wave from a blunt leading edge. The intersection results in further displacement of the bow shock wave and the formation of a supersonic jet contained between two shear layers and submerged within the subsonic shock layer between the body and the bow shock wave. A jet bow shock is produced when the jet impinges on the surface creating a small region of stagnation heating. The grid system used is shown in Figure 3 and is intended to simulate the test case of Reference [6] including the cylinder and a 7.5° shock generator wedge. There are three blocks in the grid system. The first

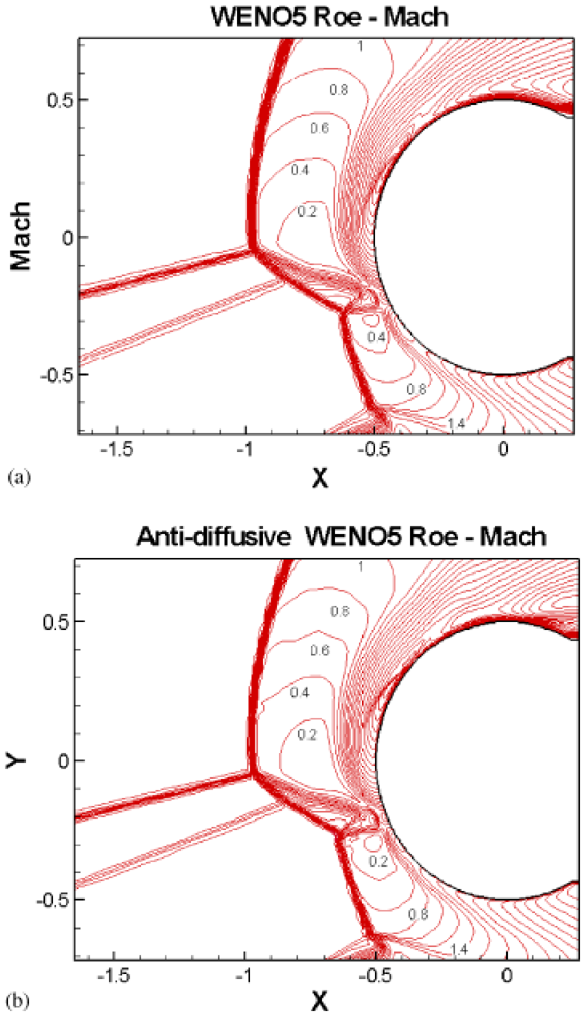

Figure 15. Mach number contours using: (a) original WENO5 scheme and (b) WENO5-AD scheme.

block has 125×181 cells above the shock generator wedge, the second one 293×61 cells around the cylinder, and the third one 89×41 cells in the rear of the shock generator wedge.

Figure 4 shows $\nabla\rho$ contours for the resulting shock impingement flowfield using the original WENO5 scheme and WENO5-AD scheme, respectively. The corresponding Schlieren photograph was observed for run 21 in [6]. The Mach number, pressure, density, and entropy contours are shown in Figures 5–9, for both the WENO5 and WENO5-AD schemes. The basic flow structures, namely, the incident shock, bow shock, transmitted shock, lower bow shock are captured quite well. The two shear layers and the jet bow shock are noticeable. The two shear layers that are slip lines can be better identified by comparing the density contours and the pressure contours. Both schemes captured those flow fields rather well. The convergence histories of both WENO5 and WENO5-AD schemes for this case are shown in Figure 10. The WENO5-AD scheme converged

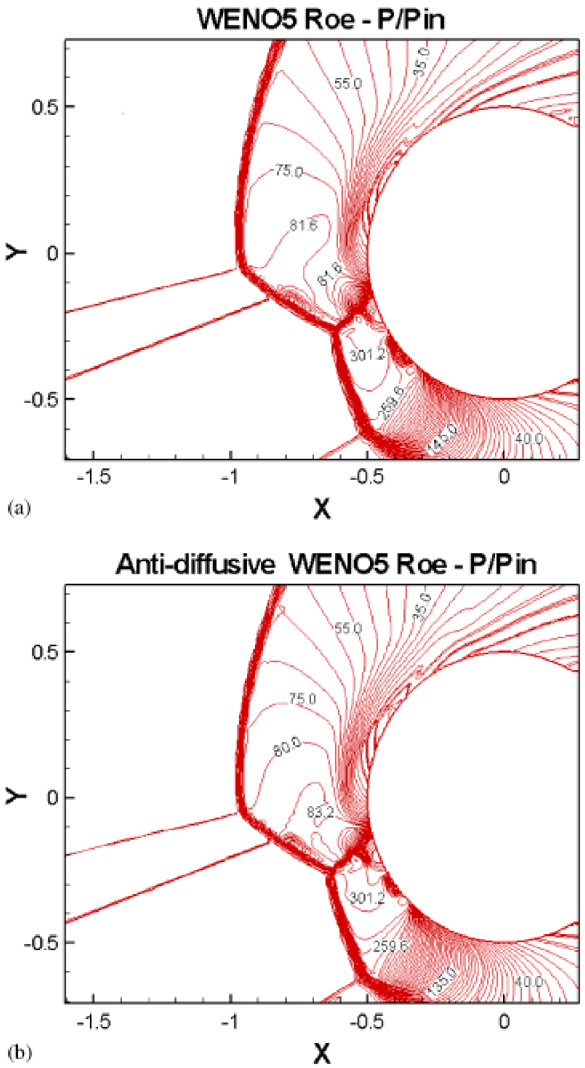

Figure 16. Pressure contours using: (a) original WENO5 scheme and (b) WENO5-AD scheme.

slightly better than that of WENO5 but with similar slow down after 6000 iteration steps. These slow convergences of both schemes may be due to the unsteadiness of type IV flow. Locally enlarged view of density contours are shown to better compare the WENO5 and WENO5-AD schemes with regard to the slip lines' resolutions. The anti-diffusive scheme seems to give slightly more noisy results while it gives better resolution and lower entropy production. The surface pressure and heat transfer rate distributions along the circumference of the cylinder for this type IV supersonic jet intersections are shown in Figures 11 and 12, respectively. These data are plotted as functions of angular position theta measured in degrees from the horizontal centerline of the

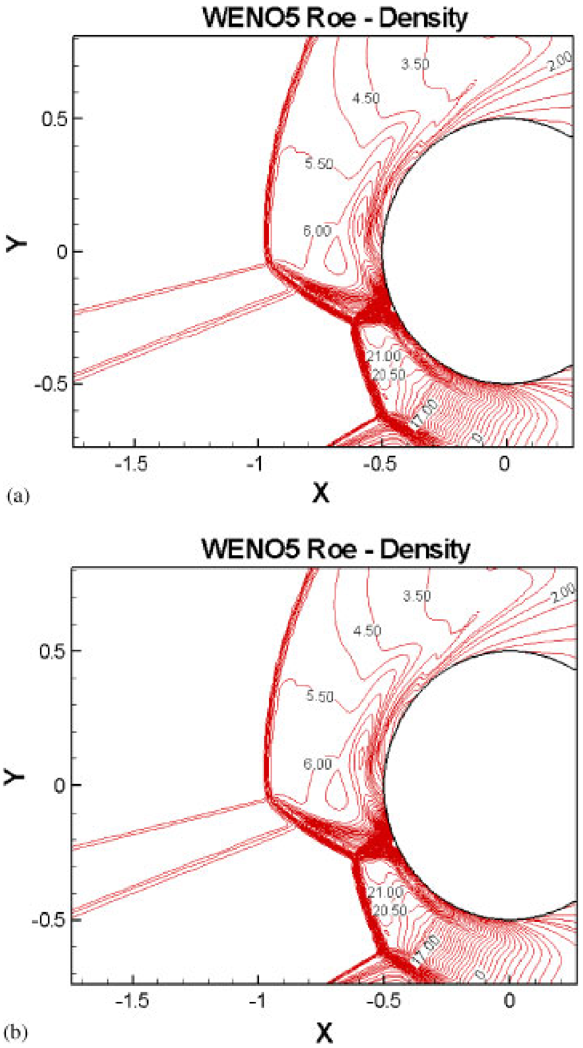

Figure 17. Density contours: (a) original WENO5 scheme and (b) WENO5-AD scheme.

cylinder [10]. Both WENO5 and WENO5-AD schemes give similar results and compare well with the experimental data. In our simulations, the maximum pressure occurs when the supersonic jet impinges near the perpendicular at $\theta \sim -19^\circ$ resulting in heat transfer rate amplification of 33.6 and 33.2, and pressure amplification of 8.1 and 8.0 for the WENO5 scheme and WENO5-AD scheme, respectively. These values compare well with the corresponding experimental values of 32 and 7.61. Here, the amplification ratio is defined as the ratio of the peak pressure or the peak heat transfer rate caused by the impingement of the shock wave interference pattern to the undisturbed free-stream stagnation pressure or heat transfer rate [6].

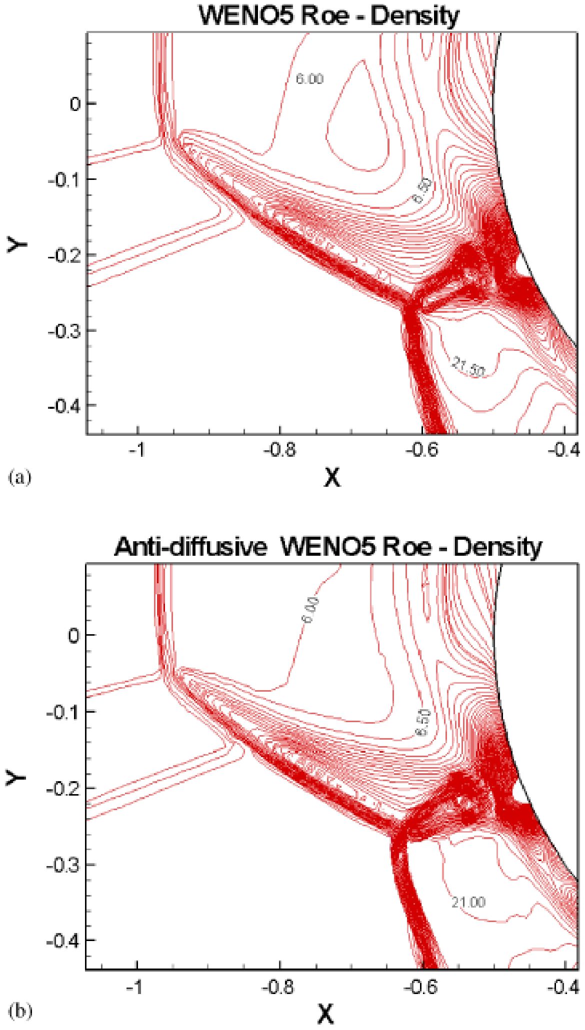

Figure 18. Density contours: (a) original WENO5 scheme, locally enlarged view and (b) WENO5-AD scheme, locally enlarged view.

6. TYPE IV INTERACTIONS GENERATED BY DUAL INCIDENT SHOCKS

The free-stream conditions chosen for the simulation were $M_\infty = 8.04$, $Re = 4.97\times 10^6$, $P_\infty =$ 0.855 kpa and $T_\infty = 122$°K. The second oblique shock wave intersects the transmitted shock wave created by the first oblique shock wave and a new shock interference pattern occurred. This new concomitant supersonic jet pattern consists of two supersonic jets separated from each other by a shear layer and they in turn are separated from the subsonic region by shear layers, as shown in Figure 2. The grid system shown in Figure 13 is intended to simulate the test section of Reference [6] including the cylinder, the first 7.5° shock generator wedge and the second 12.5°

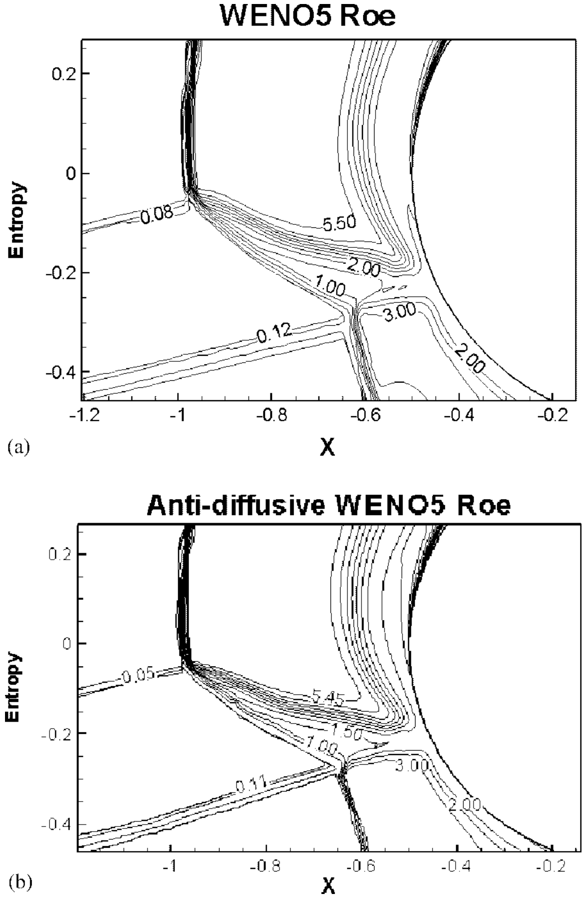

Figure 19. Entropy contours using: (a) original WENO5 scheme and (b) WENO5-AD scheme.

shock generator wedge. The structure of this grid system is similar to that used in the previous case.

In order to compare with the flow visualization experiment by Wieting for run 87 in [6], we show in Figure 14 the $\nabla\rho$ contours for the dual type IV interference pattern using original WENO5 scheme and WENO5-AD scheme, respectively. The Mach number, pressure, density, and entropy contours for the resulting shock impingement flow fields are also shown in Figures 15–19. The overall flow structures, namely the dual incident shocks, bow shock, transmitted shock, lower bow shock, the two shear layers, and the jet bow shock are captured quite well. The two shear layers that are slip lines can be better identified by comparing the density contours and the pressure contours. The convergence histories of both schemes are shown in Figure 20. Again, a rather slow rate of convergence is observed after 8000 iterations for both schemes. These slow convergences may be due to the unsteadiness of type IV flow. Locally enlarged view of density contours are shown to better compare the WENO5-R and WENO5-AD schemes with regard to the slip lines resolutions.

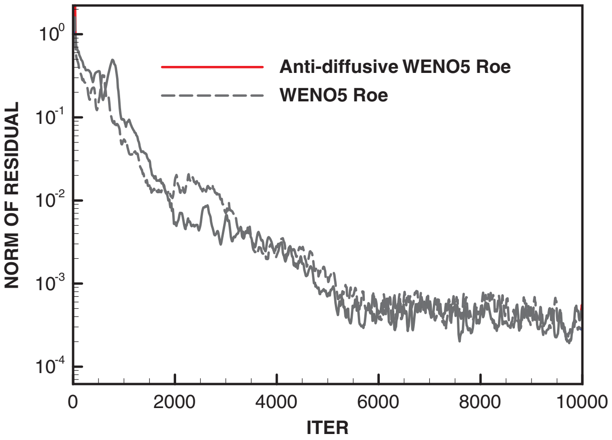

Figure 20. The convergent histories of both WENO5 and WENO5-AD.

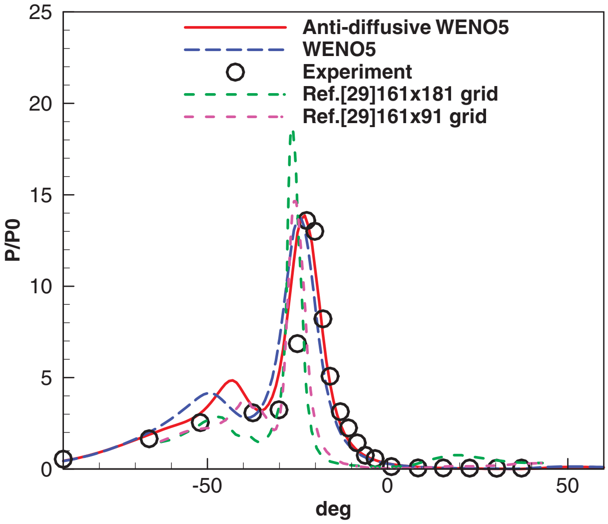

Figure 21. Pressure distributions along the circumference of the cylinder.

Again, the anti-diffusive scheme seems to give slightly more noisy results while it gives better resolution and lower entropy production. The corresponding surface pressure and heat transfer rate distributions indicate that the peak amplification ratios occur when the two incident oblique shock waves coalesced before intersecting the cylinder bow shock wave, resulting in heat transfer rate amplification of 40.2 and 40.5 for original WENO5 scheme and WENO5-AD scheme, respectively, see Figures 21 and 22. These results are compared with experiment [6] and other computational results [13] where different grids were used and laminar flow was computed, see Figures 21 and 22.

DOI: 10.1002/fld

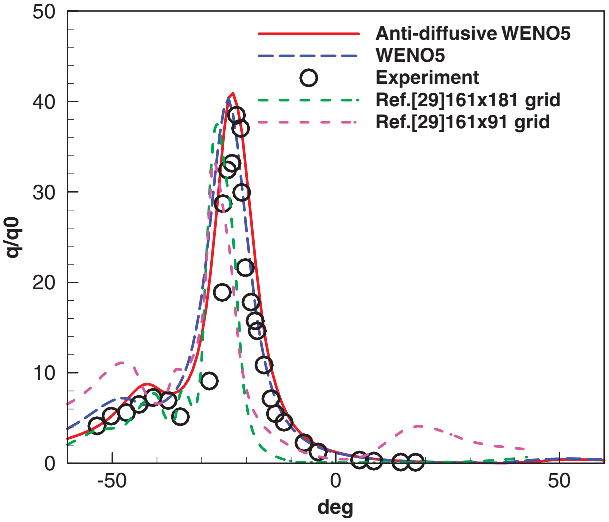

Figure 22. Heat transfer rate distributions along the circumference of the cylinder.

The present results using WENO5-AD scheme with Spalart–Allmaras turbulence model seem to give the best overall agreement with the experimental data.

7. CONCLUSIONS

Accurate computations of two-dimensional turbulent hypersonic shock–shock interactions that arise when single and dual shocks impinge on the bow shock in front of a cylinder have been carried out using a newly developed implicit anti-diffusive WENO scheme for solving the compressible Navier–Stokes equations with Spalart–Allmaras one-equation turbulence model. Simulations for experimental run 21 and run 87 of Wieting [6] are presented and compared with experimental data and other available computational results using different numerical approaches. Detailed contours of various flow properties including density, pressure, Mach number, and entropy are plotted to assist the understanding of the complex flow patterns for both WENO5 and WENO5-AD schemes. It is found that the present use of fifth-order WENO5 scheme with anti-diffusive flux corrections (WENO5-AD) for the inviscid fluxes not only enhances the resolution of contact discontinuities but also maintains the high-order accuracy of shock capturing for steady-state computation. The anti-diffusive WENO method gives smaller entropy production for both cases as expected. The main flow features of type IV shock–shock interactions including the incident shock, bow shock, transmitted shock, shear layers due to slip lines, and the resulting supersonic jet and jet bow shock are all identified and captured well. In particular, the surface pressure distribution and heat transfer rate computed by the present schemes, both the original WENO5 and the WENO5-AD schemes, are very accurate. Small discrepancy can be observed between the two WENO schemes, which may be partly due to the different slip line resolutions and partly due to the flow nature of the type IV shock–shock interactions, which may cause the flow unsteady. It is found that for all cases computed, the solutions of the present algorithms are in good agreement with the experimental data.

ACKNOWLEDGEMENTS

This work was done under the auspice of the National Science Council, Taiwan through Grant NSC-97-2212-E002-055. We thank Yeu-Ching Perng, Shih-Chang Yang, Horng-Tsair Lee, and Herng Lin of Chung-Shan Institute of Science and Technology for many useful discussions.

REFERENCES

1. Edney B. Anomalous heat transfer and pressure distributions on blunt bodies at hypersonic speeds in the presence of an impinging shock. *Report 115*, Aeronautical Research Institute, Federal Aviation Administration, Sweden, 1968.
2. Bushnell DM. Interference heating on a swept cylinder in region of intersection with a wedge at Mach 8. *NASA TN D-3094*, 1965.
3. Glass C, Wieting AR, Holden MS. Effect of leading edge weep on shock–shock interference heating at Mach 8. *AIAA Paper 89-0273*, 1989.
4. Wieting AR, Holden MS. Experimental study of shock wave interference heating on a cylindrical leading edge. *AIAA Journal* 1989; **27**:1557–1565.
5. Holden MS, Wieting AR, Moselle JR, Glass C. Studies of aerothermal loads generated in regions of shock/shock interaction in hypersonic flow. *AIAA Paper 88-0477*, 1988.
6. Wieting AR. Multiple shock–shock interference on a cylindrical leading edge. *AIAA Journal* 1992; **30**:2073–2079.
7. Grasso F, Purpura C, Chanetz B, Delery J. Type III and Type IV shock/shock interferences: theoretical and experimental aspects. *Aerospace Science and Technology* 2003; **7**:93–106.
8. Lind CA, Lewis MJ. Computational analysis of the unsteady type IV shock interaction of blunt body flows. *Journal of Propulsion and Power* 1996; **12**(1):127–133.
9. Klopfer GH, Yee HC. Viscous hypersonic shock-on-shock interaction on blunt cowl lips. *AIAA Paper 88-0233*, 1988.
10. Stewart JR, Thareja RR, Morgan K. Application of finite element and remeshing technique to shock interference on a cylindrical leading edge. *AIAA Paper 88-0368*, 1988.
11. Prabhu RK, Stewart JR, Thareja RR. Shock interference studies on a circular cylinder at Mach 16. *AIAA Paper 90-0606*, 1990.
12. Hsu K, Parpia IH. Simulation of multiple shock–shock interference patterns on a cylindrical leading edge. *AIAA Journal* 1996; **34**:764–771.
13. Holden MS, Kolly J. Measurements of heating in regions of shock/shock interaction in hypersonic flow. *AIAA Paper 95-0640*, 1995.
14. Liu XD, Osher S, Chan T. Weighted essentially non-oscillatory schemes. *Journal of Computational Physics* 1994; **115**:200–212.
15. Jiang GS, Shu CW. Efficient implementation of weighted ENO schemes. *Journal of Computational Physics* 1996; **126**:202–228.
16. Chen YN, Yang SC, Yang JY. Implicit weighted ENO schemes for the incompressible Navier–Stokes equations. *International Journal for Numerical Methods in Fluids* 1999; **31**(4):747–765.
17. Yang JY, Yang SC, Chen YN, Hsu CA. Weighted ENO schemes for the three-dimensional incompressible Navier–Stokes equations. *Journal of Computational Physics* 1998; **146**:464–487.
18. Perng YC, Yen RH, Yang JY. Implicit weighted ENO schemes for the Euler equations. *Computational Fluid Dynamics Journal* 1999; **8**:216–227.
19. Yang JY, Perng YC, Yen RH. Implicit weighted essentially non-oscillatory schemes for the compressible Navier–Stokes equations. *AIAA Journal* 2001; **39**:2082–2090.
20. Despres B, Lagoutiere F. Contact discontinuity capturing schemes for linear advection, compressible gas dynamics. *Journal of Scientific Computing* 2001; **16**:479–524.
21. Bouchut F. An anti-diffusive entropy scheme for monotone scalar conservation law. *Journal of Scientific Computing* 2004; **21**:1–30.

DOI: 10.1002/fld

22. Xu Z, Shu CW. Anti-diffusive flux corrections for high-order finite difference WENO scheme. *Journal of Computational Physics* 2005; **205**:458–485.
23. Henrick AK, Aslam TD, Powers JM. Mapped weighted essentially non-oscillatory schemes. *Journal of Computational Physics* 2005; **207**:542–567.
24. Zhang SH, Shu CW. A new smoothness indicator for the WENO schemes and its effect on the convergence to steady-state solutions. *Journal of Scientific Computing* 2007; **31**:273–305.
25. Hsieh TJ, Wang CH, Yang JY. Numerical experiments with several variant WENO schemes for the Euler equations. *International Journal for Numerical Methods in Fluids* 2008; **58**:1017–1039.
26. Yang JY, Hsieh TJ, Wang CH. Implicit WENO schemes with anti-diffusive flux for the compressible viscous flow computations. *AIAA Journal* 2009; accepted for publication.
27. Spalart PR, Allmaras SR. A one-equation turbulence model for aerodynamic flows. *AIAA Paper 92-0439*, 1992.
28. Bardina JE, Huang PG, Coakley TJ. Turbulence model vadiation, testing and development. *NASA-TM-110446*, April 1997.
29. Yoon S, Jameson A. Lower–upper symmetric-Gauss–Seidel method for the Euler and Navier–Stokes equations. *AIAA Journal* 1988; **26**:1025–1026.

DOI: 10.1002/fld